A NOVEL VARIATIONAL MODEL FOR RETINEX IN PRESENCE OF SEVERE NOISES

Lu Liu[1], *Zhi-Feng Pang*[2], *Yuping Duan*[1*]

[1] Center for Applied Mathematics, Tianjin University
[2] School of Mathematics and Statistics, Henan University

ABSTRACT

Retinex theory deals with compensation for illumination effects in images, which is usually an ill-posed problem. The existence of noises may severely challenge the performance of Retinex algorithms. Therefore, the main aim of this paper is to present a general variational Retinex model to effectively and robustly restore images corrupted by both noises and intensity inhomogeneities. Our strategy is to simultaneously recover the noise-free image and decompose it into reflectance and illumination component. The proposed model can be solved efficiently using the Alternating Direction Method of Multiplier (ADMM). Numerous experiments are conducted to demonstrate the advantages of the proposed model with Retinex illusions and medical image bias field correction for images in presence of Gaussian noise or impulsive noise.

Index Terms— Retinex, intensity inhomogeneity, denoising, image decomposition, high-order model, ADMM

1. INTRODUCTION

The Retinex theory [1] addresses the problem of decomposing the illumination from the reflectance in the given images. Such problem also exists in medical image processing, the so-called intensity inhomogeneity, which leads to the intensity variation even for the same tissue within an image. It makes other image analysis techniques such as segmentation, registration, etc., that relying on the assumption of uniform intensity, impossible to identify the region correctly.

Various implementations and algorithms have been studied for Retinex problem. Path-based methods were originated by Land and McCann [1] and further studied in [2, 3]. Homomorphic filtering type Retinex algorithms modeled the reflectance as a low-pass version of the given image based on a convolution with a wide Gaussian kernel [4, 5]. In PDE-based models and variational formulations, Morel *et al.* [6] formulated the illumination as a spatially smooth image and the reflectance as a piecewise constant image, which was further solved as a Poisson equation by Fast Fourier Transform (FFT). Based on the assumption of the spatial smoothness of the illumination, Kimmel *et al.* [7] proposed a variational model by penalizing on the reflectance. Ng and Wang [8] proposed a similar model by penalizing both the reflectance and illumination images. Ma *et al.*[9] developed a Total Variation (TV) [10] based model to extract the reflectance image with a data term in gradient field. Zosso *et al.* [11, 12] further extended the TV-based Retinex models to a unified non-local formulation. Recently, Duan *et al.* [13, 14] investigated variational models for Retinex using L_0 pseudo norm to regularize the reflectance image. Liang and Zhang [15] proposed a convex Retinex model, which decompose the gradient field of images into salient edges and relatively smoother illumination field.

1.1. Summary of Previous Methods

To set up the Retinex problem mathematically, we focus on decomposing a given image I into the reflection component R and the illumination component L, which satisfies $I(x,y) = R(x,y) \cdot L(x,y)$ for $(x,y) \in \Omega$, $\Omega \subset \mathbb{R}^2$ being the domain of the image. Actually, most Retinex algorithms were proposed in the logarithmic domain by $i = \log I$, $l = \log L$, $r = \log R$, and thereby $i = l + r$. Besides, there may be additional assumptions on r and l, e.g., the box constraint $\mathcal{B}_r =]-\infty, 0]$ and $\mathcal{B}_l = [i, +\infty[$ are introduced for r and l under the assumption that $R \in (0, 1]$ in [8].

In real applications, intensity inhomogeneities and noises may simultaneously exist in given images, such as MR images, ultrasound images etc.. Although various algorithms have gained great success in dealing with Retinex problems, these methods paid little attention to the noises contained in the given images. Especially, after taken the logarithmic transform, the distribution of the noise is also changed, which makes the noise even harder for modeling. Therefore, when noise is severe, these algorithms may fail to restore the reflection image with high quality.

1.2. Our Contributions

In this paper, we propose a general variational model for images in presence of both Retinex illusion and severe noises. More specifically, we recover the image by a TV regularization and a data fidelity term derived according to the distribution of the noises, and then decompose the restored im-

* Corresponding author: yuping.duan@tju.edu.cn. The work is supported by the 1000 Talents Program for Young Scientists of China, the Ministry of Science and Technology of China ("863" Program: 2015AA020101), and NSFC 11526208. Dr. Z.-F. Pang was partially supported by National Basic Research Program of China (973 Program No.2015CB856003) and NSFC (Nos.U1304610 and 11401170).

age into reflectance and illumination. Similar to [15], first- and second-order TV regularization are implemented for reflectance and illumination, respectively. Furthermore, we propose an efficient algorithm based on an alternating direction method of multiplier, all subproblems of which can be efficiently solved by either closed-form solution or the fast nonlinear iteration methods such as the Newton-type methods. We conclude the new features of our Retinex model as follows

- Our framework can be easily extended to other Retinex models, such as Ng and Wang's Retinex model [8], L_0 regularized Mumford-Shah model [13, 14], etc..
- Our proposed model is capable to deal with different types of noises, such as Gaussian noise, impulsive noise and Poisson noise etc., as long as we modify the data fidelity term according to the noise distribution.

2. PROBLEM FORMULATION

2.1. HoTVL1 Retinex Model

Based on the primary goal of Retinex theory, Liang and Zhang [15] proposed the HoTVL1 model as follows

$$\begin{aligned}\min_{r,l}\ \Big\{&\frac{1}{2}\int_\Omega (i-r-l)^2dx+\frac{\tau}{2}\int_\Omega l^2dx\\&+\alpha\Big(\int_\Omega \mid\nabla r\mid dx+\beta\int_\Omega\mid\nabla^2 l\mid dx\Big)\Big\},\end{aligned}\tag{1}$$

where the first- and second-order TV are used to regularize the reflectance and illumination, respectively. Compared to [8], HoTVL1 model (1) used the high-order regularization for illumination component to guarantee smoother solutions, which was shown effectively by the numerical implementations.

2.2. The Proposed Model

Suppose the given images are corrupted by both intensity inhomogeneity and noises. We consider to simultaneously recover the noise-free image and decompose it into reflectance image and illumination image. More specifically, we propose a novel Retinex model by combining the HoTVL1 model (1) and the data fidelity term derived according to different noise models. We use the additive Gaussian noise as an example, and obtain the following minimization problem

$$\begin{aligned}&\min_{u,r,l}\ \frac{1}{2}\|I-u\|_2^2+\alpha\|\nabla u\|_1+\beta\|\nabla r\|_1+\gamma\|\nabla^2 l\|_1,\\&\text{s.t., } u=e^v,\ v=r+l.\end{aligned}\tag{2}$$

Since there is a log transformation, we assume that the constraint for u is $\mathcal{B}_u = (0,+\infty[$. Obviously, the above constrained problem can be also applied to other noise models by using a suitable data fidelity term, e.g., $\|I-u\|_1$ for impulsive noise.

3. MINIMIZATION ALGORITHM

In order to simplify (2), we define some new notations and auxiliary variables as follows

$$\boldsymbol{x}=\begin{bmatrix}r\\l\end{bmatrix},\ \boldsymbol{y}=\begin{bmatrix}\boldsymbol{p}\\\boldsymbol{q}\end{bmatrix},\ A=[\mathrm{Id},\mathrm{Id}],\ L=\begin{bmatrix}\nabla & 0\\0 & \nabla^2\end{bmatrix}.$$

We further define the following functionals,

$$G(u)=\frac{1}{2}\|I-u\|_2^2+\alpha\|\nabla u\|_1,\quad H(\boldsymbol{y})=\|\boldsymbol{y}\|_{1,\beta,\gamma},$$

where $\|\boldsymbol{y}\|_{1,\beta,\gamma}=\beta\|\boldsymbol{p}\|_1+\gamma\|\boldsymbol{q}\|_1$. As a result, the minimization problem (2) can be rewritten as follows

$$\min_{u,v,\boldsymbol{x},\boldsymbol{y}}\ G(u)+H(\boldsymbol{y}),\quad \text{s.t., } u=e^v,\ v=A\boldsymbol{x},\ \boldsymbol{y}=L\boldsymbol{x}.\tag{3}$$

Therefore, the corresponding augmented Lagrangian functional of (3) is given as

$$\begin{aligned}\mathcal{L}(u,v,\boldsymbol{x},\boldsymbol{y};\Lambda_1,\Lambda_2,\boldsymbol{\Lambda}_3)&=G(u)+H(\boldsymbol{y})+\langle\Lambda_1,u-e^v\rangle\\&+\frac{\nu_1}{2}\|u-e^v\|_2^2+\langle\Lambda_2,v-A\boldsymbol{x}\rangle+\frac{\nu_2}{2}\|v-A\boldsymbol{x}\|_2^2\\&+\langle\boldsymbol{\Lambda}_3,\boldsymbol{y}-L\boldsymbol{x}\rangle+\frac{\nu_3}{2}\|\boldsymbol{y}-L\boldsymbol{x}\|_2^2,\end{aligned}\tag{4}$$

where ν_1, ν_2, ν_3 are positive constants, and Λ_1, Λ_2, $\boldsymbol{\Lambda}_3=\begin{bmatrix}\boldsymbol{\Lambda}_p\\\boldsymbol{\Lambda}_q\end{bmatrix}$ are the Lagrange multipliers.

The minimization problem (4) is solved by alternatively minimizing the variable u, v, $\boldsymbol{x}$, $\boldsymbol{y}$. In each iteration, the other three sets of variables are fixed with values obtained from the previous iteration. We discuss the solution to each set of variables separately as follows.

3.1. Subproblem 1: computing u

The sub-minimization problem w.r.t. the variable u can be written as follows

$$\min_u\ G(u)+\langle\Lambda_1,u\rangle+\frac{\nu_1}{2}\|u-e^v\|_2^2.\tag{5}$$

By introducing a new variable $\boldsymbol{h}=\nabla u$ and applying the augmented Lagrangian method, we can obtain the following saddle-point problem

$$\begin{aligned}\max_{\boldsymbol{h}}\min_u\ \alpha\|\boldsymbol{h}\|_1+\frac{1}{2}\|I-u\|_2^2+\frac{\nu_1}{2}\|u-(e^v-\frac{\Lambda_1}{\nu_1})\|_2^2\\+\langle\Lambda_4,\boldsymbol{h}-\nabla u\rangle+\frac{\nu_4}{2}\|\boldsymbol{h}-\nabla u\|_2^2.\end{aligned}\tag{6}$$

According to [16], the variable u and $\boldsymbol{h}$ can be solved efficiently by FFT and the closed-form solution, respectively. Firstly, we give the solution to u directly as follows

$$u=\mathcal{F}^{-1}\Big(\frac{\mathcal{F}(g)-\mathcal{F}(D_x^-)\mathcal{F}(\Lambda_4^1+\nu_4h^1)-\mathcal{F}(D_y^-)\mathcal{F}(\Lambda_4^2+\nu_4h^2)}{(1+\nu_1)\mathcal{I}-\nu_4\big(\mathcal{F}(D_x^-)\mathcal{F}(D_x^+)+\mathcal{F}(D_y^-)\mathcal{F}(D_y^+)\big)}\Big),$$

where $g=I-\Lambda_1+\nu_1e^v$ and D_x^-, D_y^-, D_x^+, D_y^+ denote the backward and forward difference operators with the periodic boundary condition. Besides, there is a projection step in each iteration due to the box constraint on u.

On the other hand, the variable $\boldsymbol{h}$ can be computed by

$$\boldsymbol{h}=\max\big(0,1-\frac{\alpha}{\nu_4}\frac{1}{\|\boldsymbol{w}\|_1}\big)\boldsymbol{w},$$

where $\boldsymbol{w}=\nabla u-\frac{\boldsymbol{\Lambda}_4}{\nu_4}$. More details can be found in [16].

3.2. Subproblem 2: computing v

The sub-minimization problem w.r.t. the variable v is obtained as

$$\min_{v} \langle \Lambda_1, -e^v \rangle + \frac{\nu_1}{2}\|u - e^v\|_2^2 + \langle \Lambda_2, v \rangle + \frac{\nu_2}{2}\|v - A\boldsymbol{x}\|_2^2, \quad (7)$$

the optimality condition of which gives us a nonlinear equation. We denote

$$g(v) := -\Lambda_1 e^v + \nu_1 e^{2v} - \nu_1 u e^v + \Lambda_2 + \nu_2(v - r - l). \quad (8)$$

Based on the basic Newton method, we compute v by

$$v^{k+1} = v^k - g(v^k)/g'(v^k),$$

where $g'(v) = 2\nu_1 e^{2v} - \Lambda_1 e^v - \nu_1 u e^v + \nu_2$. It requires the inner iterations for solving v, where the iteration number are fixed as 10 in the numerical implementation.

3.3. Subproblem 3: computing $\boldsymbol{x}$

The sub-minimization problem w.r.t. the variable $\boldsymbol{x}$ is given as

$$\min_{\boldsymbol{x}} \langle \Lambda_2, -A\boldsymbol{x} \rangle + \frac{\nu_2}{2}\|v - A\boldsymbol{x}\|_2^2 + \langle \boldsymbol{\Lambda}_3, -L\boldsymbol{x} \rangle + \frac{\nu_3}{2}\|\boldsymbol{y} - L\boldsymbol{x}\|_2^2, \quad (9)$$

which can be rewritten in terms of r and l as

$$\begin{aligned} \min_{r,l} \; & \langle \Lambda_2, -r - l \rangle + \frac{\nu_2}{2}\|v - r - l\|_2^2 + \langle \boldsymbol{\Lambda}_p, -\nabla r \rangle \\ & + \frac{\nu_3}{2}\|\boldsymbol{p} - \nabla r\|_2^2 + \langle \boldsymbol{\Lambda}_q, -\nabla^2 l \rangle + \frac{\nu_3}{2}\|\boldsymbol{q} - \nabla^2 l\|_2^2. \end{aligned} \quad (10)$$

Both the variable r and l can be solved by FFT, the solutions of which are given as

$$r = \mathcal{F}^{-1}\Big(\frac{\mathcal{F}(m) - \mathcal{F}(D_x^-)\mathcal{F}(\boldsymbol{\Lambda}_p^1 + \nu_3 p^1) - \mathcal{F}(D_y^-)\mathcal{F}(\boldsymbol{\Lambda}_p^2 + \nu_3 p^2)}{\nu_2 \mathcal{I} - \nu_3\big(\mathcal{F}(D_x^-)\mathcal{F}(D_x^+) + \mathcal{F}(D_y^-)\mathcal{F}(D_y^+)\big)}\Big),$$

where $m = \Lambda_2 + \nu_2 v - \nu_2 l$, and

$$l = \mathcal{F}^{-1}\Big(\frac{\mathcal{F}(n) + \nu_3 \mathcal{F}(H^*)\mathcal{F}(q) + \mathcal{F}(H^*)\mathcal{F}(\boldsymbol{\Lambda}_q)}{\nu_2 \mathcal{I} + \nu_3 \mathcal{F}(H^*)\mathcal{F}(H)}\Big),$$

where $n = \Lambda_2 + \nu_2 v - \nu_2 r$.

3.4. Subproblem 4: computing $\boldsymbol{y}$

The sub-minimization problem w.r.t. the variable $\boldsymbol{y}$ gives us

$$\min_{\boldsymbol{y}} H(\boldsymbol{y}) + \langle \boldsymbol{\Lambda}_3, \boldsymbol{y} \rangle + \frac{\nu_3}{2}\|\boldsymbol{y} - L\boldsymbol{x}\|_2^2, \quad (11)$$

which can be rewritten by $\boldsymbol{p}$ and $\boldsymbol{q}$ as

$$\begin{aligned} \min_{\boldsymbol{p},\boldsymbol{q}} \; & \beta\|\boldsymbol{p}\|_1 + \gamma\|\boldsymbol{q}\|_1 + \langle \boldsymbol{\Lambda}_p, \boldsymbol{p} \rangle + \frac{\nu_3}{2}\|\boldsymbol{p} - \nabla r\|_2^2 \\ & + \langle \boldsymbol{\Lambda}_q, \boldsymbol{q} \rangle + \frac{\nu_3}{2}\|\boldsymbol{q} - \nabla^2 l\|_2^2. \end{aligned} \quad (12)$$

Similarly to the sub-minimization problem of $\boldsymbol{h}$, we can obtain the closed-form solution to $\boldsymbol{p}$ and $\boldsymbol{q}$ as

$$\boldsymbol{p} = \max\big(0, 1 - \tfrac{\beta}{\nu_3}\tfrac{1}{\|\boldsymbol{s}\|_1}\big)\boldsymbol{s}, \qquad \text{with } \boldsymbol{s} = \nabla r - \frac{\boldsymbol{\Lambda}_p}{\nu_3};$$

$$\boldsymbol{q} = \max\big(0, 1 - \tfrac{\gamma}{\nu_3}\tfrac{1}{\|\boldsymbol{t}\|_1}\big)\boldsymbol{t}, \qquad \text{with } \boldsymbol{t} = Hl - \frac{\boldsymbol{\Lambda}_q}{\nu_3}.$$

In the end of each iteration, we update the Lagrange multipliers accordingly

$$\begin{aligned} \Lambda_1 &\leftarrow \Lambda_1 + \nu_1(u - e^v); \\ \Lambda_2 &\leftarrow \Lambda_2 + \nu_2(v - A\boldsymbol{x}); \\ \boldsymbol{\Lambda}_3 &\leftarrow \boldsymbol{\Lambda}_3 + \nu_3(\boldsymbol{y} - L\boldsymbol{x}). \end{aligned}$$

4. NUMERICAL EXPERIMENTS

In this section, we compare our model with the HoTVL1 model [15] and L0MS model [14] in order to demonstrate the advantages of our model in dealing with noises and intensity inhomogeneity.

There are several parameters in our model (2), i.e., the regularization parameters α, β, γ and the penalty parameter μ. The regularization parameter α is one of the most critical parameters in our model, which is relevant to the noise level contained in the test images. In the numerical tests, we choose α from $\alpha = 0.001$ to $\alpha = 0.1$ as the noise increases. The parameter β is used to regularize the reflectance solution r. For test images with different intensity inhomogeneity, we choose β from $\beta = 0.001$ to $\beta = 0.2$. The parameter γ is used to enforce the smoothness of the illumination l. For different test images, we can simply fix γ as $\gamma = 0.08$. All penalty parameters ν_i, $i = 1, 2, 3, 4$, are set to $\nu_i = 0.2$.

4.1. Examples of Brain Images

Example 1: Brain Images. We select two slices from the T1 brain volume with 5% noise and 40% intensity non-uniformity, which are downloaded from McGill BrainWeb: http://www.bic.mni.mcgill.ca/brainweb/. The input images, the corrected images of our model together with the results of the HoTVL1 model and L0MS model are shown in Fig. 1(a), (b), (c), (d), respectively. To quantitatively evaluate the performance of the three methods, we compute both Peak Signal to Noise Ratio (PSNR) and Mean Squared Error (MSE) and list the values in Table 1. It can be observed that both PSNR and MSE of our model are significantly better than the other two methods, which demonstrate its advantage in removing the noises and intensity inhomogeneity.

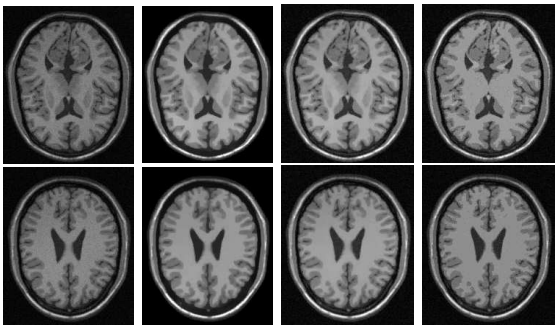

(a) Input (b) Our Model (c) HoTVL1 (d) L0MS

Fig. 1. The corrected results of our model, HoTVL1 model and L0MS model on T1 brain images.

Table 1. PSNR and MSE of T1 brain images.

		Our model	HoTVL1	L0MS
Test image 1	PSNR	30.0261	27.5423	27.4783
	MSE	0.0010	0.0018	0.0018
Test image 2	PSNR	30.7099	28.8196	28.5584
	MSE	0.0008	0.0013	0.0014

Example 2: Stable Performance for Intensity Inhomogeneity and Noises. We select one slice from the T1 brain volume and generate 10 different images by adding Gaussian white noise of mean 0 and variance 0.001 and intensity inhomogeneity of different profiles. Two selected results are displayed in Fig. 2. In the experiment, we fix the parameters of the three methods for all 10 images, which are given in the figure. In Fig. 3 (a), we plot the PSNR of the 10 images for the three methods, which demonstrate that our model gives the best denoising results. Simultaneously, Fig. 3 (b) gives the energy decay of our model for the first image in Fig. 2 to illustrate the convergence of the proposed method.

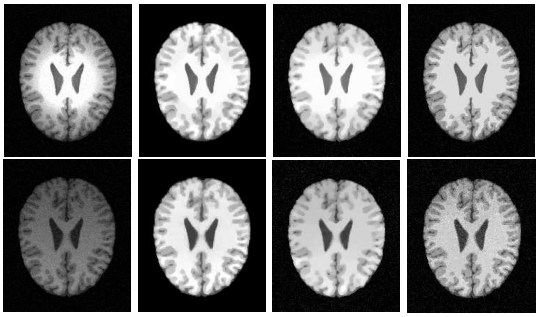

(a) Input (b) Our Model (c) HoTVL1 (d) L0MS

Fig. 2. Performances of three methods with noises and intensity inhomogeneity of different profiles. The parameters for our model are $\alpha = 0.03$, $\beta = 0.01$, $\gamma = 0.08$, $\mu = 0.2$ and for HoTVL1 model are $\alpha = 0.15$, $\beta = 10$, $\mu = 0.02$, $\tau = 1e{-}03$ and for L0MS model are $\alpha = 0.05$, $\mu = 1.0$,$\sigma = 4.0$.

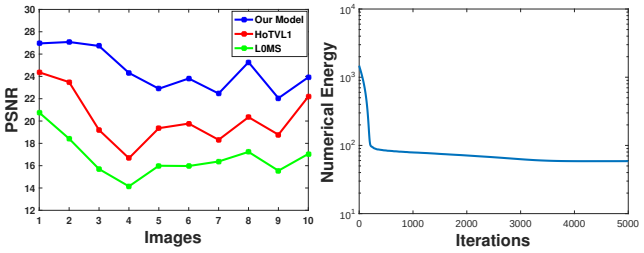

(a) (b)

Fig. 3. Comparison of three models in terms of PSNR and the numerical energy of our model for the first image in Fig. 2.

On the other hand, we evaluate the performance of bias correction of our model using the coefficient of variations (CV) to quantify the degree of intensity inhomogeneity. We define CV for each tissue T (WM, GM and CSF) as $\mathrm{CV(T)} = \frac{\sigma(\mathrm{T})}{\mu(\mathrm{T})} \times 100\%$, where $\sigma(\mathrm{T})$ and $\mu(\mathrm{T})$ are the standard deviation and the mean of the intensities in the tissue T. The CV values of White Matter (WM), Gray Matter (GM) and Cerebrospinal Fluid (CSF) are evaluated on the bias corrected images of the three methods and plotted by boxplots in Fig.4. We can see that CV of our model is better than HoTVL1 model, which is better than L0MS model.

4.2. Examples of Retinex Illusion Images

Example 3: Checkboard and Cube Images. We start with Retinex illusion examples with the checkboard shadow image and the Logvineko's cube shadow illusion image. We add the Gaussian white noise of mean 0 and variance 0.001 to both images. The results of the HoTVL1 model and our model are displayed in Fig. 5. We observe that the HoTVL1 model fails to remove all noises contained in the test images.

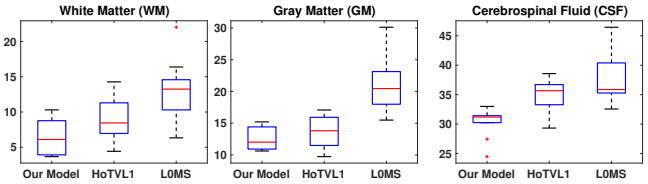

Fig. 4. Comparison of the performance in terms of CV(%).

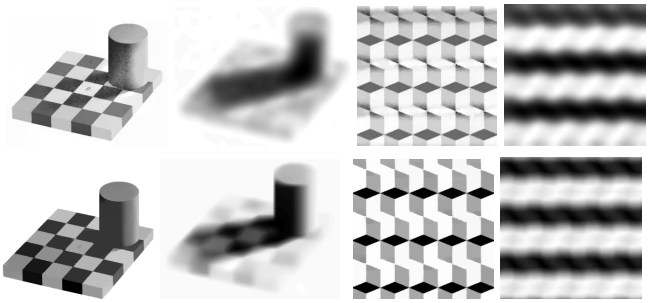

(a) r (b) l (c) r (d) l

Fig. 5. Decomposition comparison of the checkboard example. The parameters for test images of our model are $\alpha = 0.01$, $\beta = 0.04$, and the HoTVL1 model are $\alpha = 0.15$, $\beta = 15$. Row 1 and row 2 are the results of HoTVL1 and our model, respectively.

Example 4: Test of Impulsive Noise. As we claimed, our model is flexible to noises of different modalities. In this example, we apply the impulsive noises into the checkboard image and define $G(u) = \|I - u\|_1 + \alpha\|\nabla u\|_1$. Similarly, the minimization problem can be solved efficiently by augmented Lagrangian method. Fig. 6 presents the results of checkboard image, which is corrupted by 20% impulsive noise. It demonstrates the advantages of our model in dealing with different noises.

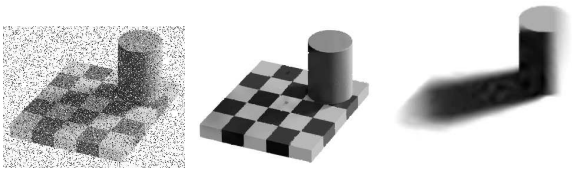

(a) Input image (b) r by our model (c) l by our model

Fig. 6. Denoising the checkboard image containing impulsive noise. The parameters are $\alpha = 0.5$, $\beta = 0.065$, $\gamma = 0.08$, $\mu = 0.5$.

5. CONCLUSION AND FUTURE WORKS

In this paper, we have presented an efficient model for Retinex problem, which was developed for images corrupted by both intensity inhomogeneities and noises. We designed an efficient alternating minimization algorithm, where all subproblems can be solved by the closed-form solutions and the basic Newton method. The framework can be easily applied to other Retinex models and is shown robust with different noise models. Various numerical results were implemented to demonstrate the advantages of our model over the existing method including [14, 15] for Retinex applications.

6. REFERENCES

[1] Land E.H. and McCann J.J., "Lightness and retinex theory," *Journal of the Optical Society of America*, vol. 61, no. 1, pp. 1–11, 1971.

[2] Marcelo Bertalmío, Vicent Caselles, and Edoardo Provenzi, "Issues about retinex theory and contrast enhancement," *International Journal of Computer Vision*, vol. 83, no. 1, pp. 101–119, 2009.

[3] Daniele Marini and Alessandro Rizzi, "A computational approach to color adaptation effects," *Image and Vision Computing*, vol. 18, no. 13, pp. 1005–1014, 2000.

[4] OD Faugeras, "Digital image color processing within the framework of a human visual system," *IEEE Trans. on ASSP*, vol. 27, pp. 380–393, 1979.

[5] Daniel J Jobson, Zia-ur Rahman, and Glenn A Woodell, "Properties and performance of a center/surround retinex," *IEEE transactions on image processing*, vol. 6, no. 3, pp. 451–462, 1997.

[6] Jean Michel Morel, Ana Belen Petro, and Catalina Sbert, "A pde formalization of retinex theory," *IEEE Transactions on Image Processing*, vol. 19, no. 11, pp. 2825–2837, 2010.

[7] Ron Kimmel, Michael Elad, Doron Shaked, Renato Keshet, and Irwin Sobel, "A variational framework for retinex," *International Journal of computer vision*, vol. 52, no. 1, pp. 7–23, 2003.

[8] Michael K Ng and Wei Wang, "A total variation model for retinex," *SIAM Journal on Imaging Sciences*, vol. 4, no. 1, pp. 345–365, 2011.

[9] Wenye Ma, Stanly Osher, and Selim Esedoglu, "A tv bregman iterative model of retinex theory.," *Inverse Problems & Imaging*, vol. 6, no. 4, pp. 697–708, 2012.

[10] Leonid I Rudin, Stanley Osher, and Emad Fatemi, "Nonlinear total variation based noise removal algorithms," *Physica D: Nonlinear Phenomena*, vol. 60, no. 1, pp. 259–268, 1992.

[11] Dominique Zosso, Giang Tran, and Stanley Osher, "A unifying retinex model based on non-local differential operators," in *IS&T/SPIE Electronic Imaging*. International Society for Optics and Photonics, 2013, pp. 865702–865702.

[12] Dominique Zosso, Giang Tran, and Stanley Osher, "Non-local retinex—a unifying framework and beyond," *SIAM Journal on Imaging Sciences*, vol. 8, no. 2, pp. 787–826, 2015.

[13] Yuping Duan, Huibin Chang, Weimin Huang, and Jiayin Zhou, "Simultaneous bias correction and image segmentation via L_0 regularized mumford-shah model," in *2014 IEEE International Conference on Image Processing (ICIP)*. IEEE, 2014, pp. 6–40.

[14] Duan Yuping, Chang Huibin, Huang Weimin, Zhou Jiayin, Lu Zhongkang, and Wu Chunlin, "The L_0 regularized mumford-shah model for bias correction and segmentation of medical images," *IEEE Transactions on Image Processing*, vol. 24, no. 22, pp. 3927–3937, 2015.

[15] Liang Jingwei and Zhang Xiaoqun, "Retinex by higher order total variation L^1 decomposition," *Journal of Mathematical imaging and vision*, vol. 52, no. 3, pp. 345–355, 2015.

[16] Wu Chunlin and Tai Xuecheng, "Augmented lagrangian method, dual methods, and split bregman iteration for rof, vectorial tv, and high order models," *SIAM Journal on Imaging Sciences*, vol. 3, no. 3, pp. 300–339, 2010.